

RESEARCH ARTICLE

# On the application of hole-selective $\text{MoO}_x$ as full-area rear contact for industrial scale p-type c-Si solar cells

Hisham Nasser<sup>1</sup>  | Fırat Es<sup>1,2</sup> | Mona Zolfaghari Borra<sup>1,3</sup>  | Emel Semiz<sup>1,4</sup>  | Gamze Kökbudak<sup>1,3</sup> | Efe Orhan<sup>1</sup> | Raşit Turan<sup>1,3</sup> 

<sup>1</sup>The Center for Solar Energy Research and Applications (GÜNAM), Middle East Technical University (METU), Ankara, 06800, Turkey

<sup>2</sup>Kalyon Güneş Teknolojileri Üretim A.Ş., Başkent OSB, Malıköy, Ankara, Turkey

<sup>3</sup>Micro and Nanotechnology Graduate Program of Natural and Applied Sciences, Middle East Technical University (METU), Ankara, 06800, Turkey

<sup>4</sup>Science and Technology Policy Studies (METU-TEKPOL), Middle East Technical University (METU), Ankara, 06800, Turkey

## Correspondence

Hisham Nasser and Raşit Turan, Center for Solar Energy Research and Applications (GÜNAM), Middle East Technical University, Çankaya, 06800 Ankara, Turkey.  
Email: nasser@metu.edu.tr;  
turann@metu.edu.tr

## Funding information

Scientific and Technological Research Council of Turkey (TÜBİTAK), Grant/Award Numbers: 217M087 and 217M203

## Abstract

We present the feasibility of integrating substoichiometric molybdenum oxide ( $\text{MoO}_x$ ) as hole-selective rear contact into the production sequence of industrial scale p-type crystalline silicon (c-Si) solar cells. Thin films of  $\text{MoO}_x$  are deposited directly on p-type c-Si by thermal evaporation at room temperature. It is found that  $\text{Ag}/\text{MoO}_x/\text{p-type c-Si}$  rear contact structure exhibits low contact resistivity and modest surface recombination current density. The attained peak efficiency ( $\eta$ ) of the fabricated solar cells is 17.65% with  $V_{oc}$  of 626 mV,  $J_{sc}$  of 36.8 mA/cm<sup>2</sup>, and fill factor (FF) of 76.63%. Next, a complete loss analysis of a  $\text{MoO}_x/\text{p-type Si}$  heterojunction solar cell is carried out for the first time by using Quokka simulation software that employs characteristics of different layers which constitute the fabricated solar cell. Based on this loss analysis, the dominant loss mechanisms are defined and a roadmap to attain the desired highest possible efficiency from industrial scale p-type c-Si solar cells with full-area  $\text{MoO}_x$  hole-collecting rear contact is explored.

## KEYWORDS

dopant free, hole-selective contact,  $\text{MoO}_x$ , passivating contacts, p-type c-Si, solar cells, synergetic loss analysis

## 1 | INTRODUCTION

Crystalline silicon (c-Si) photovoltaic (PV) technology has achieved power conversion efficiencies (PCEs) with values approaching the practical achievable limit of 29%.<sup>1</sup> Ultra-high PCE values up to 26.7% are already achieved with interdigitated back-contact silicon heterojunction (IBC-SHJ) design that employs intrinsic and doped hydrogenated amorphous silicon thin films (a-Si:H) as passivation carrier selective contacts (CSCs).<sup>2</sup> Recently, p-type c-Si solar cells with a polycrystalline Si on oxide (POLO-IBC) have reached to a remarkably high PCE of 26.1%.<sup>3</sup> Though these designs have reached an advanced stage in the development of efficient c-Si solar cells, there still exist several challenges such as thermal instability, strong parasitic light absorption by the utilized thin films, especially a-Si:H due to its rather small band gap, and the used inevitable complicated deposition processes by PECVD followed by photolithography and/or laser steps.

Recently, there has been a considerable attention to use alternative dopant-free CSCs for c-Si solar cells due to their unique work function values, considerably large band gap, simpler contact formation, and ease of production by simpler techniques.<sup>4–12</sup> These dopant-free CSCs have shown to remove fundamental limitations associated with doped Si layers such as Auger recombination, parasitic light absorption, and free carrier absorption.<sup>13–15</sup> Several dopant-free CSCs layers have been used in c-Si solar cells such as metal oxides, metal fluorides, or metal nitrides.<sup>14,16</sup> In general, the band gap and work function of dopant-free CSCs induce a band alignment with the adjacent Si and metal contacts in such a way that these layers allow one type of photogenerated charge carriers to be transported while blocking the other.<sup>14,16–23</sup>

Among different extensively explored dopant-free CSCs, substoichiometric molybdenum oxide ( $\text{MoO}_x$ ) thin films, with high work function exceeding 5.5 eV and band gap well above 3 eV, have been

successfully integrated on the front sides of SHJ solar cells on 4-cm<sup>2</sup> n-type substrates, as a substitute of p-type a-Si:H, resulting in an impressive efficiency of up to 23.5%.<sup>24</sup> Thin films of MoO<sub>x</sub> can be deposited by several simple fabrication methods, at room or low processing temperature (<200°C), such as thermal evaporation,<sup>8,25,26</sup> atomic layer deposition (ALD),<sup>27</sup> sputtering,<sup>28</sup> or solution process technique.<sup>29</sup> Our simulation studies, using Silvaco TCAD tool, have demonstrated that high-efficiency values of ~22% and ~25% can be achieved by placing MoO<sub>x</sub> at the rear (back surface field)<sup>30</sup> and front side (emitter),<sup>31</sup> respectively, of SHJ solar cells based on n-type c-Si wafers. Moreover, thin films of MoO<sub>x</sub> have been integrated into the fabrication of dopant-free asymmetric heterocontacts (DASH) solar cells<sup>6,11</sup>; 19.42% efficiency was reported for DASH solar cells on n-type c-Si wafer with MoO<sub>x</sub> and lithium fluoride (LiF) as hole and electron-selective contacts placed at the front and rear side, respectively.<sup>11</sup> Recently, DASH solar cell with an efficiency of 20.7% was demonstrated with MoO<sub>x</sub> as front side hole-selective contact and with stack of titanium dioxide (TiO<sub>2</sub>) and LiF as electron-selective rear contact.<sup>6</sup> In both designs, the wafers were passivated by thin films of intrinsic a-Si:H, and cell area was limited to 4 cm<sup>2</sup>. Notably, our simulation studies on DASH solar cells, with MoO<sub>x</sub> and TiO<sub>2</sub> on n-type c-Si wafer passivated with a-Si:H, have shown that efficiencies of up to 22.64% are possible.<sup>12</sup> Several attempts to apply MoO<sub>x</sub> on large area solar cells on n-type wafers have been demonstrated. Six-inch n-type SHJ solar cells with efficiency of 16.1% were achieved by utilizing electron beam evaporated MoO<sub>x</sub> with intrinsic a-Si:H on the front side and intrinsic/n-type a-Si:H as back surface field stack.<sup>32</sup> Spinelli et al. have reported large area (9.2 × 9.2 cm<sup>2</sup>) SHJ solar cell with front side thermally evaporated MoO<sub>x</sub> with intrinsic a-Si:H passivation layer, reaching an efficiency of 18.1%, with n-poly-Si/SiO<sub>2</sub> stack as back surface field.<sup>33</sup> Recently, Cho et al. have demonstrated an impressive efficiency of 19.3% from 4 × 4 cm<sup>2</sup> SHJ with front side thermally evaporated MoO<sub>x</sub> with intrinsic a-Si:H and intrinsic/n-type a-Si:H as back surface field stack.<sup>22</sup>

On the other hand, there are few works reported in literature where hole-collecting MoO<sub>x</sub> is utilized in p-type c-Si solar cell architectures.<sup>34,35</sup> An efficiency of 20.4% has been realized on high quality float zone (FZ), p-type c-Si wafers featuring photolithographically defined, through Al<sub>2</sub>O<sub>3</sub>/SiN<sub>x</sub>, MoO<sub>x</sub> dot contacts with ~5% rear fraction.<sup>34</sup> Efficiency of 16.4% has been achieved in simple rear side full-area MoO<sub>x</sub>/p-type (FZ) c-Si solar cell.<sup>35</sup> However, thus far, all demonstrations of MoO<sub>x</sub>/p-type solar cells are limited to small area (≤4 cm<sup>2</sup>) and using industrially infeasible processing steps as well as exploiting the advantages of high quality FZ wafers.

In this work, we present high-efficiency industrial scale p-type (Cz) c-Si solar cells, featuring full-area hole-collecting MoO<sub>x</sub> rear contact as a potential substitute to conventional back surface field counterparts. The MoO<sub>x</sub>/p-type semi-DASH solar cells are fabricated by following the common processing sequence of solar cells based on p-type wafers and using industrial equipment. In order to demonstrate the potential limit of the fabricated industrial scale p-type/MoO<sub>x</sub> solar cells, we have run synergetic efficiency gain analysis "SEGA" using Quokka 2.<sup>36,37</sup> SEGA considers different electrical, resistive,

recombination, and optical losses on an equal basis. It determines the minor and dominant loss mechanisms of each parameter of the fabricated solar cell. By identifying the main losses, via this analysis, a roadmap to attain the desired highest efficiency from the proposed solar cell design was traced.

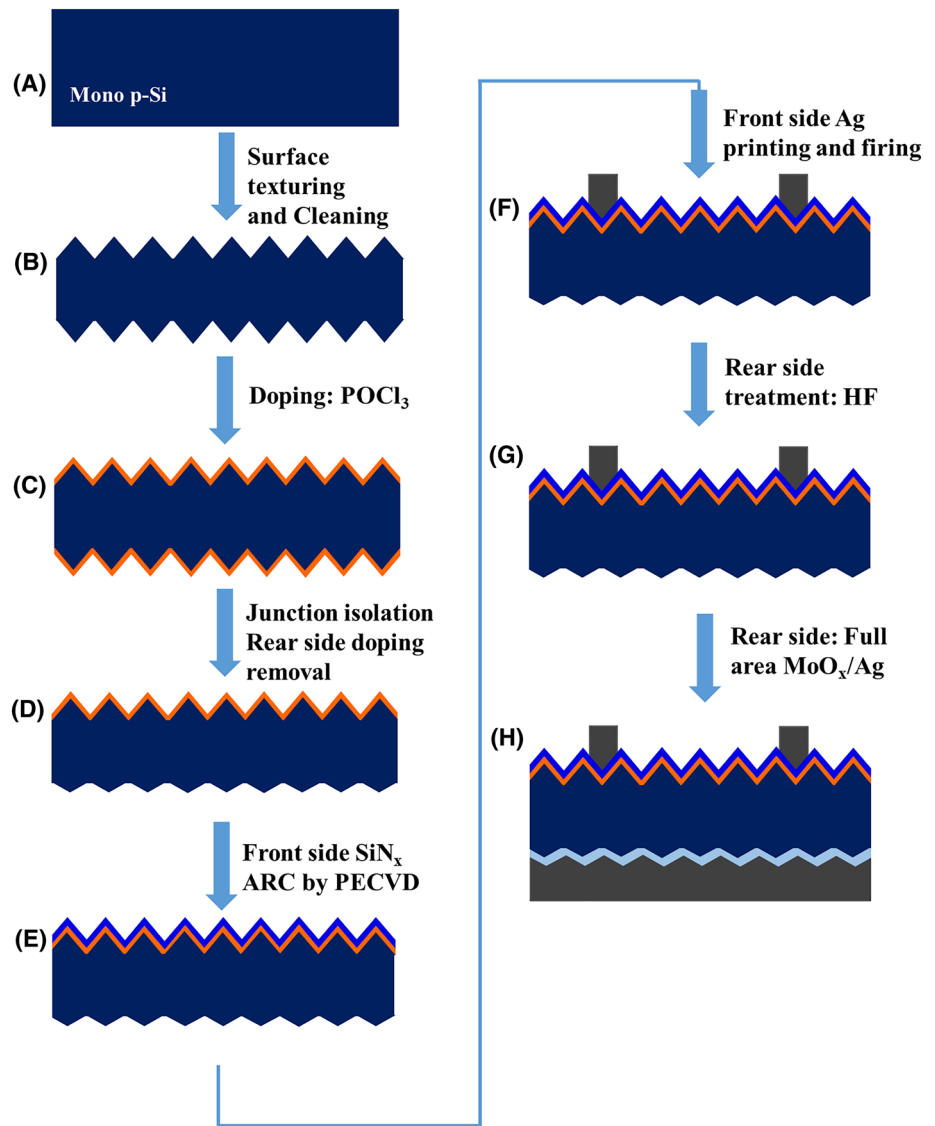
## 2 | MATERIAL AND METHODS

Solar cells were fabricated on 156 × 156 mm<sup>2</sup> large p-type (Cz) mono-c-Si solar wafers (1–3 Ω-cm, diamond wire cut) with 180-μm thickness. Figure 1 outlines the fabrication flow using industrial scale solar cell production processing steps and industrial equipment for p-type c-Si solar cells.

First, the wafers were double side textured by potassium hydroxide (KOH) with organic additive agent to form random micropyramids on both surfaces of the wafers that reduce the total reflection and improve light trapping (Figure 1B). After texturing, organic and metal cleaning were implemented via ozone treatment and HF/HCl baths, respectively. Textured and cleaned wafers were doped to create n+ front emitter in an atmospheric solid state diffusion furnace which employs phosphorus oxychloride (POCl<sub>3</sub>) as precursor (Figure 1C). Then, single side of the wafers was exposed to HF:HNO<sub>3</sub>:H<sub>2</sub>SO<sub>4</sub> bath for junction isolation and the removal of doped layer at the rear (Figure 1D) using an industrial fully automated wet bench (RENA InPilot). The phosphosilicate glass (PSG) on the front was removed by HF based acidic solution in successive baths of the same wet bench. Silicon nitride (SiN<sub>x</sub>) was deposited on the front side as antireflective coating (ARC) and passivation layer (Figure 1E) in an industrial plasma-enhanced chemical vapor deposition (PECVD) tool. Front side metal contacts, configured as four Ag busbars together with fingers, were formed by screen printing and fast-firing step (Figure 1F). Right after removal of the native oxide at the rear surface by dilute HF (Figure 1G), without altering front side SiN<sub>x</sub>/Ag stack, ~20-nm-thick MoO<sub>x</sub> thin films were thermally evaporated, from stoichiometric MoO<sub>3</sub> powder (>3 N purity) at a rate of ~0.3 Å/s, and ~1-μm-thick thermally evaporated Ag contacts were deposited subsequently in the same thermal evaporation system without breaking the vacuum (Figure 1H). A set of reference solar cells without MoO<sub>x</sub> layer, with only ~1-μm-thick Ag rear contact, was also fabricated.

The thickness, band gap, and optical properties of MoO<sub>x</sub> were extracted using variable angle spectroscopic ellipsometry (VASE). The measurements were performed on MoO<sub>x</sub>, deposited on clean and polished c-Si wafer, using SE (GESSE-Semilab Sopra) in the 1.23–4.00 eV range and fitted using Cauchy with Urbach Tail.<sup>38,39</sup> Contact resistivity ( $\rho_c$ ) was extracted by depositing MoO<sub>x</sub>/Ag, on polished p-type c-Si (1–3 Ω-cm) wafers according to the method devised by Cox and Strack by considering the recently developed approximations.<sup>40,41</sup> The rear side of the measurement structure is made ohmic by evaporating full-area MoO<sub>x</sub>/Ag and is assumed to have a negligible contribution to the total measured resistance, rendering the measured  $\rho_c$  an upper limit of Ag/MoO<sub>x</sub>/p-type c-Si  $\rho_c$ . Corresponding dark current–voltage (*I*–*V*) measurements were

**FIGURE 1** Conceptual structure and fabrication steps of the fabricated p-type crystalline silicon (c-Si) solar cells with full-area  $\text{MoO}_x/\text{Ag}$  hole-collecting rear contact



collected at room temperature ( $\sim 24^\circ\text{C}$ ) using a 2425-Keithley source-meter. The excess carrier lifetimes and rear contact recombination parameter ( $J_0$  rear contact) were measured, on symmetrically  $\text{MoO}_x$  coated double side polished p-type wafers with thickness of  $275\ \mu\text{m}$  and resistivity of  $1\text{--}3\ \Omega/\text{cm}$ , by quasi-steady-state photoconductance (QSSPC) using a Sinton Instruments WCT120 photoconductor tool. The lifetimes were recorded at excess minority carrier density ( $\Delta n$ ) of  $5 \times 10^{15}\ \text{cm}^{-3}$ . Performance of p-type c-Si/ $\text{MoO}_x$  and reference solar cells were evaluated from  $I$ - $V$  measurements under standard 1-sun condition ( $1000\ \text{mW}/\text{m}^2$ , AM 1.5 spectrum,  $25^\circ\text{C}$ ), by a calibrated AAA class type solar simulator. External quantum efficiency (EQE) and front side reflection ( $R$ ) were measured by a PV characterization system with an integrating sphere (Bentham Instruments, PVE300).

### 3 | RESULTS AND ANALYSES

The rear side of p-type wafers features roughened micropyramids with few microns in size, as shown in Note S1 and Figure S1;

therefore, in order to ensure complete surface coverage of Si surface, the thickness of  $\text{MoO}_x$  is adjusted to  $\sim 20\ \text{nm}$ . The corresponding optical properties, extracted from SE measurement and fitting, with ultra-high fitting accuracy ( $R^2 = 0.999$ ), are given in Figure 2. Details of SE analysis are given in Note S2, Figure S2, and Table S1. Fitting SE measured parameters resulted in film thickness of  $21.4\ \text{nm}$  and exhibited a refractive index ( $n$ ) and extinction coefficient ( $k$ ) of  $1.90$  and  $0.0046$ , respectively, at the wavelength of  $632.8\ \text{nm}$ , with a band gap of  $\sim 3.18\ \text{eV}$ . The transmission spectrum of  $\text{MoO}_x$ , displayed in Figure 2B, has high weighted transmittance ( $W_T$ , calculated by integration with AM 1.5 solar spectral irradiance) of  $86.85\%$ . As can be seen,  $\text{MoO}_x$  has high total transmission over a broad wavelength range from  $400$  to  $1200\ \text{nm}$ . This is in line with the low  $k$ , indicating unpronounced absorption both in the visible and in the infrared, with more than  $90\%$  transmission, portions of the spectrum. The relatively pronounced absorption, lower transmission, at wavelengths shorter than  $400\ \text{nm}$  becomes an issue when  $\text{MoO}_x$  is placed as a window layer in solar cell designs. This requires the use of even thinner layers, of less than  $5\ \text{nm}$ ,<sup>24</sup> to further reduce parasitic light absorption. Importantly,

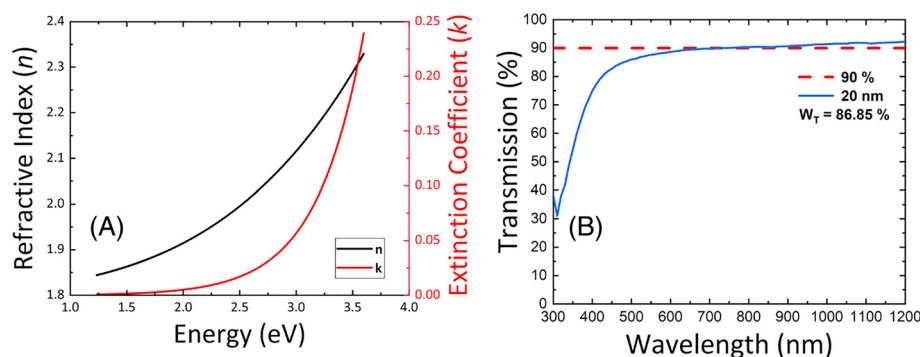


**FIGURE 2** Optical properties of 20-nm-thick  $\text{MoO}_x$ : (A) refractive index and extinction coefficient and (B) total transmission

$\text{MoO}_x$  has low absorption in the infrared. These results indicate that when applying  $\text{MoO}_x$  as hole-selective layer at the solar cell rear side, where only longer wavelengths can reach, parasitic light absorption within the film remains weak. Moreover, the low refractive index value of 1.9 is useful to block the excitation of surface plasmon polaritons, for sufficiently thick films, and thus reduces parasitic plasmonic infrared light absorption by the rear metal contact.

The measured minority carrier lifetime and contact resistivity are displayed in Figures 3 and 4, respectively. When  $\text{MoO}_x$  is deposited on p-type c-Si wafer, an effective lifetime ( $\tau_{\text{eff}}$ ) of 29.75  $\mu\text{s}$ , which translates into implied open-circuit voltage ( $iV_{\text{oc}}$ ) of 603 mV, was obtained. Although the passivation quality of  $\text{MoO}_x$  is clearly not as good as the widely used thin films to passivate Si surface, such as intrinsic a-Si:H, polycrystalline Si on oxide, or  $\text{Al}_2\text{O}_3/\text{SiN}_x$ , it shows a certain degree of surface passivation. This passivation is due to the

band alignment that  $\text{MoO}_x$  induces when in junction with p-type c-Si which results information of an accumulation layer at the interface where electrons are repelled away as well as the presence of a thin  $\text{SiO}_2$  (<2 nm) interfacial layer between Si and  $\text{MoO}_x$  that is formed during  $\text{MoO}_x$  deposition.<sup>22,42</sup> Notably,  $\text{MoO}_x$  exhibits  $J_0$  rear contact value of  $\sim 310 \text{ fA/cm}^2$  in addition to a low  $\rho_c$  of  $53 \text{ m}\Omega/\text{cm}^2$ . The  $J_0$  rear contact, extracted from lifetime measurements according to Kane and Swanson technique,<sup>43</sup> directly reflects the recombination parameter of  $\text{MoO}_x$ /p-type c-Si due to the presence of a strong accumulation layer induced by  $\text{MoO}_x$  at the surface with high hole concentration. This value is close to the reported value of  $\sim 200 \text{ fA/cm}^2$  for  $\text{MoO}_x$  deposited on p-type c-Si with wafer resistivity of  $\sim 2.1 \Omega/\text{cm}$ .<sup>44</sup> Here, it is important to underline that  $J_0$  value of bare, nonmetalized,  $\text{MoO}_x$ /p-type c-Si has been found to have scarce dependence on the presence of metal overlayer, usually used to mimic the real device contact

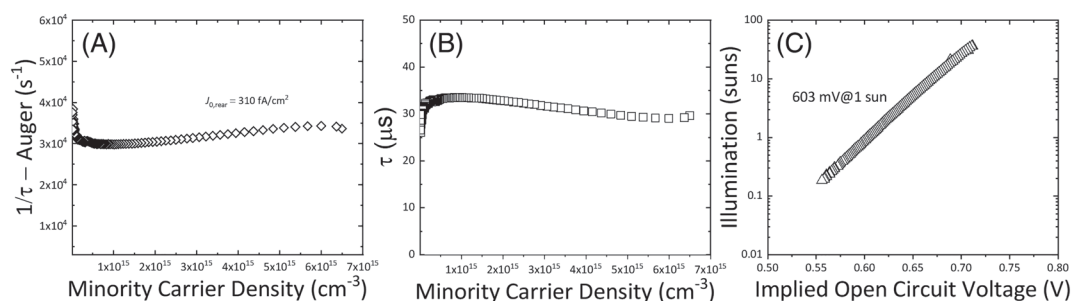


**FIGURE 3** UREQuasi-steady-state photoconductance (QSSPC) lifetime measurements of  $\text{MoO}_x$  on p-type crystalline silicon (c-Si) wafers to extract (A)  $J_0$  rear and (B) effective lifetime at  $\Delta n = 5 \times 10^{15} \text{ cm}^{-3}$ , and corresponding  $iV_{\text{oc}}$  at 1 sun

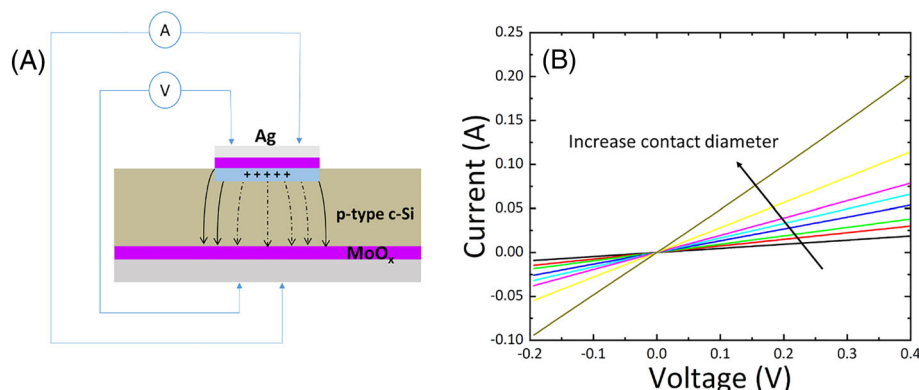


**FIGURE 4** (A) Cox and Strack contact structure and (B) current-voltage measurements varying contact pad diameter to extract  $\rho_c$  of  $\text{Ag}/\text{MoO}_x$ /p-type crystalline silicon (c-Si)

structure during  $J_0$  extraction.<sup>44</sup> Therefore, it is safe to state that  $J_{0 \text{ rear}}$ , extracted from lifetime measurements of bare  $\text{MoO}_x/\text{p-type c-Si}$  symmetric test structure, represents  $J_{0 \text{ rear contact}}$ . Notably, the extracted  $J_{0 \text{ rear contact}}$  is much lower than that obtained from a direct metal contact with moderately doped c-Si which incurs interface with severe carrier recombination resulting in  $J_{0 \text{ contact}} \geq 10^6 \text{ fA/cm}^2$ .<sup>45</sup> High  $J_{0 \text{ contact}}$  is known to limit  $V_{oc}$  values of solar cells, featuring moderately doped wafers with full-area metal contact, to  $\sim 600 \text{ mV}$ . The obtained  $\text{MoO}_x/\text{p-type}$  contact recombination parameter value is close to the values obtained from conventional boron-diffused  $\text{Si}^{45}$  which further proves that  $\text{MoO}_x$  can act as an alternative efficient hole extraction layer.

On the other hand, the obtained low  $\rho_c$  of  $53 \text{ m}\Omega/\text{cm}^2$  is not the lowest that can be obtained from  $\text{MoO}_x/\text{p-type c-Si}$  contact structure. Bullock et al. have obtained  $\rho_c$  of 1 and  $0.2 \text{ m}\Omega/\text{cm}^2$ , respectively, from 10-nm  $\text{MoO}_x$  on p-type c-Si ( $2.1 \text{ }\Omega/\text{cm}$ ) and 5-nm  $\text{MoO}_x$  on p-type c-Si where in both cases palladium was used as the metal contact.<sup>44</sup> This difference between our  $\rho_c$  and the lowest obtained value of  $0.2 \text{ m}\Omega/\text{cm}^2$  is because  $\text{MoO}_x/\text{Si}$  heterojunction is highly affected by the  $\text{MoO}_x$  thickness, the material of the used overlayer metal contact, Si wafer base resistivity, and the doping nature. The increase in  $\rho_c$  with  $\text{MoO}_x$  thickness is related to the high bulk resistivity of  $\text{MoO}_x$ . The material of the metal used may influence the degree of accumulation at the  $\text{MoO}_x/\text{p-type Si}$  interface due to possible work function misalignments or the differences in chemical reaction between  $\text{MoO}_x$  and different metals.<sup>46</sup> Dependence of  $\rho_c$  on Si resistivity, for the same doping type, is likely a consequence of the current flow across the  $\text{Ag}/\text{MoO}_x$  and  $\text{MoO}_x/\text{c-Si}$ , as illustrated in Cox and Strack structure in Figure 4, and the change in Si Fermi level position influencing

the overall band alignment induced at the  $\text{MoO}_x$  and Si interface.<sup>8,31</sup> Although  $\text{MoO}_x$  exhibits an n-type character, the work function of n-type and p-type c-Si with respect to that  $\text{MoO}_x$ , results in the formation of an inversion or accumulation layer at the  $\text{MoO}_x/\text{Si}$  interface, respectively.<sup>31,47</sup> In our case, the contact resistivity measured for  $\text{Ag}/\text{MoO}_x/\text{p-type c-Si}$  contact resembles the actual device rear contact structure featuring 21.39-nm-thick  $\text{MoO}_x$  and Ag as metal contact on p-type ( $1\text{--}3 \text{ }\Omega/\text{cm}$ ) Si wafer. This value is close to the reported  $\rho_c$  between  $37\text{--}45 \text{ m}\Omega/\text{cm}^2$  from 20-nm-thick  $\text{MoO}_x$  on p-type c-Si wafer, yet with gold as metal contact.<sup>48</sup> Nevertheless, the  $\rho_c$  of  $\text{MoO}_x/\text{p-type Si}$ , strong accumulation, is much lower than that obtained from  $\text{MoO}_x/\text{n-type Si}$ , strong inversion, with  $\rho_c$  in the order of  $300 \text{ m}\Omega/\text{cm}^2$ .<sup>42</sup>  $\text{MoO}_x$  forms Schottky junction with n-type c-Si<sup>8</sup> as their large work function difference induces large upward band bending which depletes the interface from majority carriers resulting in an inversion. Conversely, the work function difference with p-type c-Si is small resulting in a quasi-ohmic contact. It has been proven that extraction of photogenerated holes through carrier accumulation formed at  $\text{MoO}_x/\text{p-type c-Si}$  is more feasible than that through surface inversion induced at the  $\text{MoO}_x/\text{n-type c-Si}$ .<sup>44,49</sup> The obtained  $iV_{oc}$ ,  $J_0$ , and  $\rho_c$  values demonstrate that our  $\text{MoO}_x/\text{Ag}$  stack simultaneously acts as an efficient hole-selective and modest passivating contact to p-type c-Si wafers.

Figure 5A displays the illuminated  $I\text{--}V$  characteristics of the solar cells with  $\text{MoO}_x/\text{Ag}$  and Ag rear contacts. Corresponding detailed solar cells parameters are summarized in Table 1. The aforementioned optical, electrical, and passivation benefits of  $\text{MoO}_x$  contact resulted in an improved efficiency of p-type c-Si with full-area  $\text{MoO}_x/\text{Ag}$  as compared with the reference cell with only Ag at the rear. The cell

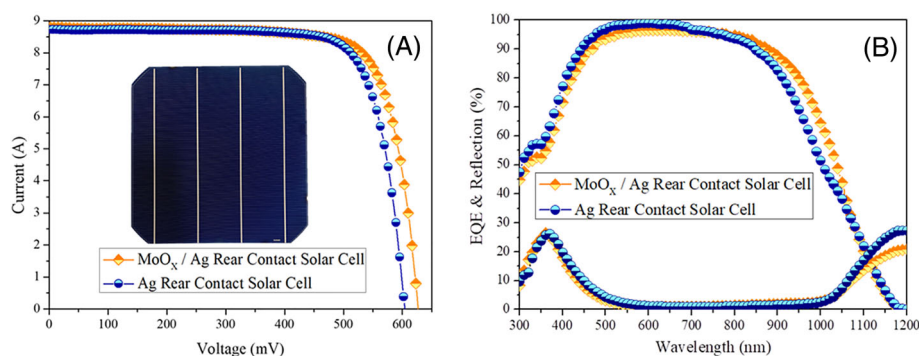


**FIGURE 5** (A) One-sun  $I\text{--}V$  characteristics of p-type crystalline silicon (c-Si) solar cell with  $\text{MoO}_x/\text{Ag}$  and reference cell with Ag at the rear, also shown photograph of the fabricated industrial scale solar cell with  $\text{MoO}_x/\text{Ag}$  rear contact, and (B) corresponding external quantum efficiency (EQE) and total reflection response of the fabricated solar cells. Note: Please check the Supporting Information for detailed analysis of  $\text{MoO}_x/\text{Ag}$  and Al-BSF based solar cells (Note S3, Figures S3–S5, and Table S2)

**TABLE 1** Photovoltaic parameters of industrial scale solar cells with and without  $\text{MoO}_x$

Cell structure	$V_{oc}$ (mV)	$J_{sc}$ ( $\text{mA}/\text{cm}^2$ )	FF (%)	$\eta$ (%)
Ag rear contact cell	605	36.50	76.30	16.80
$\text{MoO}_x/\text{Ag}$ rear contact cell (semi-DASH)	626	36.80	76.63	17.65
Enhancement	+21	+0.3	+0.33	+0.85

Abbreviation: DASH, dopant-free asymmetric heterocontacts.



with MoO<sub>x</sub>/Ag rear contact has attained  $V_{oc}$  (open-circuit voltage) = 626 mV,  $J_{sc}$  (short-circuit current density) = 36.8 mA/cm<sup>2</sup>, and fill factor (FF) = 76.63% resulting in an efficiency ( $\eta$ ) of 17.65%. The  $V_{oc}$  and FF values are significantly higher than those previously reported for a direct MoO<sub>x</sub> contact with p-type c-Si.<sup>35</sup> The low  $\rho_c$  of Ag/MoO<sub>x</sub>/p-type c-Si translates into improved FF. This value is an evidence of effective majority carrier transport through MoO<sub>x</sub> towards corresponding contact. However, overall FF can be also limited by front side doping/SiN<sub>x</sub>/Ag grid contacts recipe. Still, taking into account that both cells feature identical front side doping/metal contact recipe, the cell with MoO<sub>x</sub> has shown better FF value. It is clearly seen that the cell with an optimized MoO<sub>x</sub>/Ag rear contact has higher  $V_{oc}$  of 626 mV as compared with the reference cell without MoO<sub>x</sub>, with  $V_{oc}$  of 605 mV. Although this value is in the low range of solar cells with typical passivated contacts, it shows a certain degree of surface passivation by MoO<sub>x</sub>, as confirmed by carrier lifetime measurements via the QSSPC technique from symmetrical samples. Moreover, the band bending induced by MoO<sub>x</sub> repels minority carrier, electrons, away from the rear contact interface and thus reduce back surface recombination. The discrepancy between  $iV_{oc}$  obtained from QSSPC measurements and the  $V_{oc}$  obtained from the solar cell may be attributed to the difference in the used wafers for each case. While the wafer used to extract  $iV_{oc}$  is double side polished 275- $\mu$ m-thick wafer with 2.5  $\Omega$ /cm, the wafer used in solar cell production is as cut 180- $\mu$ m-thick wafer with 1.6  $\Omega$ /cm which experienced high temperature processes. The  $J_{sc}$  value is modest in our cells and can be further improved by optimizing the rear side reflectivity.

Figure 5B shows that EQE response increases (for wavelength  $\geq$  850 nm) along with lower total reflection (for wavelength  $\geq$  1020 nm) by inserting MoO<sub>x</sub> between Si and Ag as compared with cell with only Ag. For wavelengths between  $\sim$ 450 and  $\sim$ 900 nm, both solar cell designs exhibit similar EQE response with values higher than 95% demonstrating good front side texturing and antireflection coating (Figure 5B). The slight differences in EQE and total reflection response, at shorter wavelengths, between the two cells may arise from possible variations in SiN<sub>x</sub> deposition on different wafers. More importantly, for longer wavelengths, above  $\sim$ 870 nm, the cell with MoO<sub>x</sub>/Ag exhibits better EQE response. This improvement further demonstrates the benefits of the used hole-selective MoO<sub>x</sub> rear contact. Integrating EQE and the solar spectrum product yields a  $J_{sc}$  of 36.95 mA/cm<sup>2</sup>. This value is in good agreement with the  $J_{sc}$  value obtained from 1-sun  $I$ - $V$  measurements. In order to investigate the surface coverage of the chosen MoO<sub>x</sub> thickness, EQE mapping performed at wavelength of 900 nm, directly reflects the quality of the back side because light with this wavelength can reach the back surface. Figure 6 shows the EQE values collected at 900 nm from different coordinates of the wafer. It can be clearly seen that the EQE exhibits excellent values  $\geq$  78% over different positions of the wafer and only small area, mainly at the lower corner, shows EQE  $\approx$  70–72% which may arise from slight inhomogeneity in MoO<sub>x</sub> thickness across the wafer. The rather homogenous EQE response in the infrared confirms adequate conformal surface coverage of texturized Si wafer (i.e., no pinholes<sup>50</sup>) by the  $\sim$ 22-nm-thick MoO<sub>x</sub> contact.

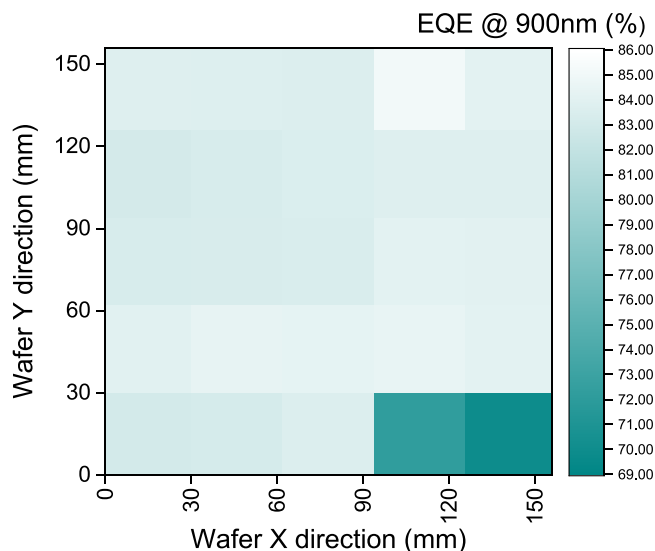


**FIGURE 6** UREExternal quantum efficiency (EQE) mapping at 900 nm of the solar cell with MoO<sub>x</sub>/Ag rear contact

After confirming the true potential of hole-selective MoO<sub>x</sub>/Ag as rear contact of p-type solar cells, the attention is steered towards investigating the loss mechanisms that hinders the overall performance of the fabricated solar cell. The input parameters used in SEGA are given in Table 2. These parameters are either measured using the corresponding measurement techniques or extracted from relevant literature. Scanning electron microscopy (SEM) imaging was referred to identify the geometrical properties of the unit cell based on half finger width. The symmetry element used in SEGA framework is given Note S4 and Figure S6. Wafer characteristics, front side doping, contact resistivity, and recombination parameters were extracted from our previous work where the used wafers and front side doping/SiN<sub>x</sub>/Ag recipe were just identical.<sup>51</sup> Remaining parameters such as diffusivity and front metal recombination were extracted from literature. The optical generation profile was calculated by transmitted spectrum and using 1D model given in Quokka 2 where we employed the SE results of MoO<sub>x</sub> and reflection spectrum of semi-DASH solar cell. For rear side, MoO<sub>x</sub>/Ag was introduced in SEGA as a contact stack layer characterized in terms of  $J_{0 \text{ rear}}$  and  $\rho_c$ .

To validate the accurate choice of input parameters used, the fabricated solar cell was first simulated. The simulated  $J$ - $V$  characteristics are displayed in Figure 7. Both fabricated and simulated  $I$ - $V$  characteristics of semi-DASH cell agrees well, with only slight deviations, as shown in the inset of Figure 8. Simulated cell resulted in +3 mV, +0.1 mA/cm<sup>2</sup>, +0.07%, and +0.15% higher  $V_{oc}$ ,  $J_{sc}$ , FF, and  $\eta$ , respectively. The slight differences between both  $I$ - $V$  characteristics prove that hole-selective MoO<sub>x</sub>/Ag stack can be adapted to SEGA platform as a contact layer.

In SEGA, deactivating each individual power loss mechanism, by setting the corresponding input parameter to its ideal value, reveals the potential efficiency gain that is hindered due to imperfect value of actual parameters.<sup>52</sup> The sum of synergistic efficiency gain from each loss mechanism leads the maximum efficiency improvement that can

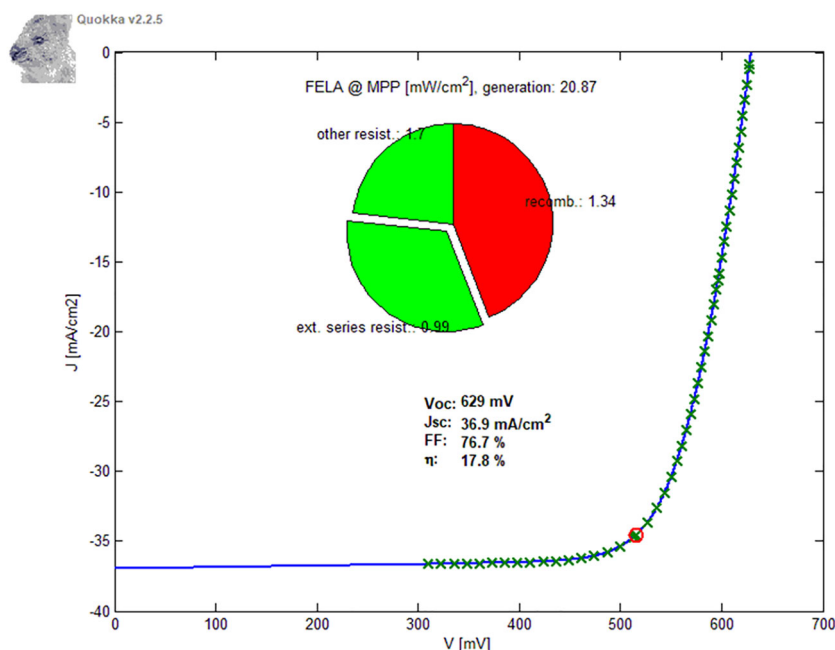
**TABLE 2** Parameters used as input to simulate the *I*–*V* characteristics of the semi-DASH cell with 17.65% efficiency

Parameter	Value	Measurement method
Cell area	700 × 700 μm <sup>2</sup>	Unit cell, fixed
Cell thickness	167 μm	SEM imaging
Emitter sheet resistance ( <i>R</i> <sub>sh</sub> )	71 Ω/□	Electrochemical capacitance voltage (ECV) profiling <sup>a</sup>
Finger width	52 μm	SEM imaging
Junction depth	605 nm	ECV profiling <sup>a</sup>
<i>J</i> <sub>0 emitter</sub>	120 fA/cm <sup>2</sup>	QSSPC <sup>a</sup>
<i>ρ</i> <sub>c front</sub>	4 mΩ/cm <sup>2</sup>	Transmission line method (TLM) <sup>a</sup>
Bulk resistance ( <i>R</i> <sub>bulk</sub> )	1.6 Ω/cm	ECV profiling <sup>a</sup>
Bulk lifetime ( <i>τ</i> <sub>bulk</sub> )	100 μs	QSSPC <sup>a</sup>
<i>J</i> <sub>0 rear contact</sub>	310 fA/cm <sup>2</sup>	QSSPC
Rear contact resistivity ( <i>ρ</i> <sub>c MoO<sub>x</sub>/Ag</sub> )	53 mΩ/cm <sup>2</sup>	<i>I</i> – <i>V</i> Cox and Strack
Series resistivity ( <i>ρ</i> <sub>series</sub> )	0.83 Ω/cm <sup>2</sup>	<i>I</i> – <i>V</i> solar simulator
Shunt resistivity ( <i>ρ</i> <sub>shunt</sub> )	1051 Ω/cm <sup>2</sup>	<i>I</i> – <i>V</i> solar simulator
Diffusivity ( <i>D</i> )	27 cm <sup>2</sup> /s	Obtained from Sproul <sup>65</sup>
Front metal recombination	7000 cm/s	Obtained from Horbelt et al. <sup>66</sup>

<sup>a</sup>From our previous work where the presented solar cells here were taken from the same batch of doping, SiN<sub>x</sub>, and front metal contact processes.<sup>51</sup> Abbreviation: DASH, dopant-free asymmetric heterocontacts; QSSPC, quasi-steady-state photoconductance; SEM, scanning electron microscopy.

be attained by avoiding these loss mechanisms. It is noteworthy that SEGA covers all losses arising from recombination; resistive, electrical, and optical properties of different layers of the cell. SEGA, therefore, depicts the improvements in efficiency for each loss mechanism arising from the properties of each constituent of the fabricated semi-DASH solar cell, as shown in Figure 8. It shows two dominating loss mechanisms, that is, synergetic optical and recombination losses in the fabricated solar cell.

All resistive electrical losses sum up to a synergetic gain of 1.25%. The dominated resistive loss is caused by front fingers and busbar resistances with a potential efficiency increase by 1.03%. This loss can be reduced by further improving front side metallization recipe or by switching to an advanced metallization configuration using higher number of busbars. An optimized front side metallization recipe is also expected to avoid the losses arising from front contact resistance which has the potential to increase the efficiency by 0.14%. Resistive losses due to bulk and emitter resistance are the second largest contributor to the 1.25% efficiency gain due to resistive losses. The rear contact resistance, MoO<sub>x</sub>/Ag, is the smallest contributor with only 0.1% potential efficiency gain. This is expected because of the low contact resistivity of rear side p-type c-Si/MoO<sub>x</sub>/Ag stack with 53 mΩ/cm<sup>2</sup>, where the area is large considering full-area MoO<sub>x</sub> surface coverage. Still, reducing the contact resistivity of p-type c-Si/MoO<sub>x</sub>/Ag stack by reducing MoO<sub>x</sub> thickness is expected to further reduce the fraction of power loss due to rear side contact.<sup>24,53</sup> Interestingly, although it is possible to achieve lower contact resistivity values from p-type c-Si/MoO<sub>x</sub>/Ag by decreasing the MoO<sub>x</sub> thickness, the potential efficiency gain will be unnoticeable. Attempts to avoid the losses due to rear contact resistance, by reducing MoO<sub>x</sub> thickness, can likely have detrimental influences on the solar cell performance due to possible poor surface coverage of texturized silicon rear surface, by ultra-thin MoO<sub>x</sub> resulting in direct Ag/Si local contact with

**FIGURE 7** Simulated *J*–*V* output of semi-dopant-free asymmetric heterocontacts (DASH) solar cell using parameters in Table 2

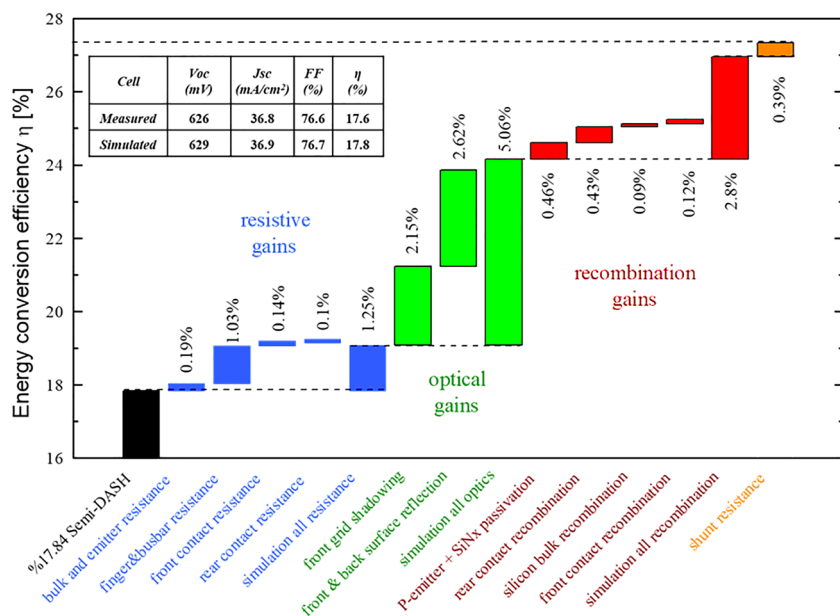



**FIGURE 8** SEGA analysis of 17.84% semi-dopant-free asymmetric heterocontacts (DASH) solar cell with MoO<sub>x</sub>/Ag rear contact. Efficiency gains are absolute %. Inset: Simulated solar obtained from experimentally measured parameters of different layers, agree well with that measured from the light  $I$ - $V$

high resistive and recombination losses. Consequently, it can be concluded that in the design of p-type c-Si solar cell with rear side MoO<sub>x</sub> as hole-selective contact, it can be tolerable to consider thicker MoO<sub>x</sub> as long as the contact resistivity is sufficiently low. As a direct result, the weak dependency of semi-DASH solar cell efficiency on MoO<sub>x</sub> thickness ( $\leq 23$  nm, sufficiency thin) and the homogenous EQE response in the infrared (Figure 6) with this thickness suggest that the chosen MoO<sub>x</sub> thickness of  $\sim 22$  nm can be considered as the optimum in the current cell design. The cell also exhibits a shunt loss (0.39%) that can be avoided by shadow masking of the edges during formation of contacts.

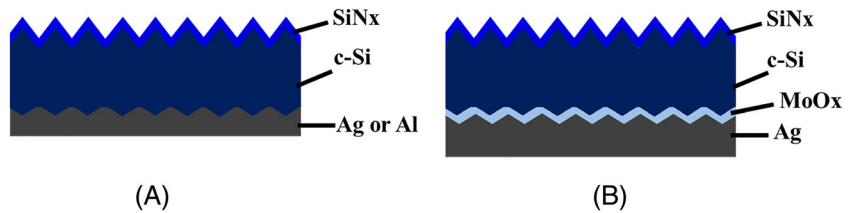
Synergetic efficiency enhancement relevant to all optical and recombination losses is 5.06% and 2.8%, respectively. Recombination losses are mainly arisen from front side emitter and passivation (0.46%) and rear contact recombination (0.43%). The first loss mechanism can be alleviated by improving the front side doping/SiNx recipe to reduce  $J_0$  emitter. The rear contact (p-type c-Si/MoO<sub>x</sub>/Ag) has relatively large  $J_0$  rear contact of 310 fA/cm<sup>2</sup> which is plausible because MoO<sub>x</sub> directly deposited on moderately doped Si surface is not expected to provide high surface passivation quality. A prerequisite to collect the potential efficiency gain due rear side passivation loss is to have the lowest achievable  $J_0$  which can be possible by inserting a passivating interlayer such as intrinsic a-Si:H<sup>14,54–56</sup> or applying MoO<sub>x</sub> in partial rear contact architectures similar to that of passivated emitter and rear contact (PERC)<sup>51,57,58</sup> solar cell designs. At this point it is important to mention that applying convenient passivation layer on Si can result in  $J_0$  well below 5 fA/cm<sup>2</sup>.<sup>14,56,59,60</sup> The contribution of remaining recombination loss mechanisms, that is, the silicon bulk and front contact recombination is smaller. The largest individual contributors to efficiency gain are the front and rear surface reflectivity with potential 2.62% followed by front metal grid shadowing with 2.15%. Avoiding grid shadowing will increase  $J_{sc}$  by 2.15% which accounts for  $36.8 \times 2.15\% = 0.79$  mA/cm<sup>2</sup> and will lead to  $J_{sc}$  (no shadowing) with

a value of 37.59 mA/cm<sup>2</sup>. However, the potential  $J_{sc}$  obtained by omitting front grid shadowing is larger than the  $J_{sc}$  of 36.95 mA/cm<sup>2</sup> calculated from EQE results because the presence of metal contacts, as in the case of  $J_{sc}$  from EQE, incurs front side recombination and resistive losses.

Finally, the attention is now on front and rear surface reflectivity as the most dominating individual loss mechanism. At shorter wavelengths, total reflection of semi-DASH solar cell is pronounced as shown in Figure 5B, with a maximum well above 25%. This wavelength range is directly related to front side reflectivity (can be termed as external reflection because rear side reflection = 0) which is governed by surface texturing and SiNx recipe. One way to avoid high front side reflection can be considering double antireflection coating designs. For wavelengths longer than 1020 nm, total reflection in Figure 5B comprises mainly reflection of rear side (escape reflection) and slightly of front side (external reflection). While external reflection is correlated to front side texturing and antireflection coating, escape reflection is the light that leaves front side of the solar cell after interacting with the wafer (partially absorbed) and internally reflected back by the rear surface. It is of note that the amount of escape reflection is also related to the fraction of light being absorbed by rear films. For rear side reflectivity, a careful analysis is therefore required. To acquire further insight on the rear reflectivity and to investigate the relation between rear side contact type and improved EQE response and also reduced total reflection (escape + external) in the infrared (Figure 5B), extensive optical simulations using wafer ray tracer<sup>61</sup> were performed as shown in Figures 10A–F and 11. The solar cell structures used in the simulations feature c-Si solar cell with front side structure similar to that of the fabricated semi-DASH cell. The rear sides are full-area metal contact (the metal being Ag or Al) and MoO<sub>x</sub>/Ag with different MoO<sub>x</sub> thicknesses ( $t = 5, 10, 20, 50$ , and 120 nm) as, respectively, displayed in Figure 9A,B. Different MoO<sub>x</sub> thicknesses were considered to optically assess corresponding infrared light



**FIGURE 9** Two-dimensional schematic representations of solar cell structures used in simulations with different rear side configurations (A) Al or Ag and (B) MoO<sub>x</sub>/Ag with different MoO<sub>x</sub> thicknesses



absorption. The structure with rear Al was introduced in the analysis to mimic the actual rear side of a conventional Al-BSF solar cell.

Similar to the behavior observed in semi-DASH solar cell, simulated total reflection in the infrared decreases by inserting 20-nm-thick MoO<sub>x</sub> between Si and Ag. Figure 10A further shows that at shorter wavelengths, escape reflection is 0, and therefore, total reflection is just the external reflection from the front side, as we mentioned before. Escape reflection becomes pronounced at wavelengths longer than ~1000 nm and again decreases by inserting 20-nm-thick MoO<sub>x</sub>, as seen in Figure 10A,B. The slight difference between total and escape reflection in the infrared wavelength range is due to the contribution of front side external reflection. However, simulated absorption in Si of the cell with only Ag, and thus simulated photogenerated current density ( $J_{ph}$ ), outperforms the 20-nm MoO<sub>x</sub>/Ag counterpart, being opposite to the observed increase in EQE. Such discrepancy can be explained by the increased parasitic absorption in the rear films of 20-nm MoO<sub>x</sub>/Ag as compared with less absorption

by Ag as seen in Figure 10D. This indicates that only 20-nm-thick MoO<sub>x</sub> is not enough to suppress, and even triggers, the penetration of evanescent waves into the metal as evident from the reduced escape reflection, exciting surface plasmon polaritons, thereby increasing the plasmonic absorption loss at the rear.<sup>62,63</sup> As a result, the observed simulated and experimental low reflection in the infrared and the relevant current loss are associated with the increased rear side parasitic absorption caused by the rear film (Figure 11) rather than being related to enhanced absorption in Si.

It is important to note that wafer ray tracer does not take into account recombination and resistive losses, and hence, simulated light absorption by silicon wafer and  $J_{ph}$  render the upper limits, especially, for the case of Al and Ag. Nevertheless, simulated absorption by Si and  $J_{ph}$  of the cell with rear Al, as the most common used rear contact in p-type c-Si solar cells, is considerably lower compared with that of Si with 20-nm-thick MoO<sub>x</sub>/Ag rear contact. Direct metal contacting with moderately doped Si inevitably incurs electrical and severe

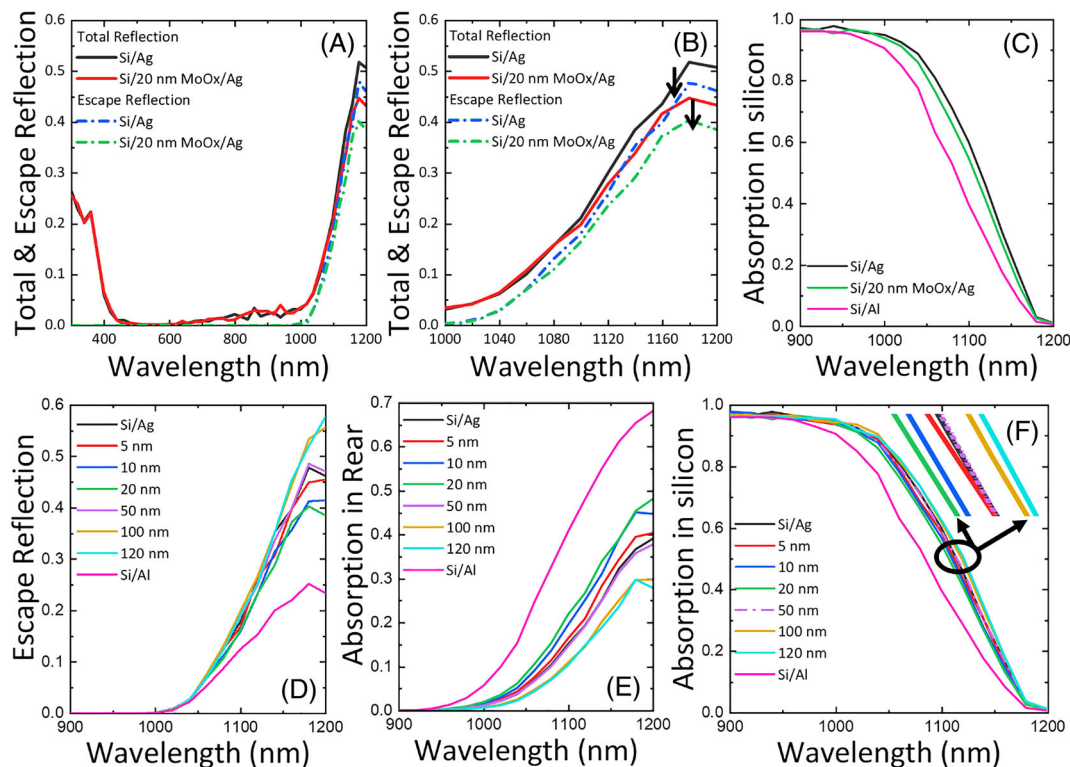


**FIGURE 10** (A,B) Simulated total and escape reflection of test structures with Ag and 20-nm-thick MoO<sub>x</sub>/Ag rear contacts and (C) corresponding light absorption in Si. (D) Escape reflection, (E) parasitic absorption in rear films, and (F) absorption in Si, varying with MoO<sub>x</sub> thickness

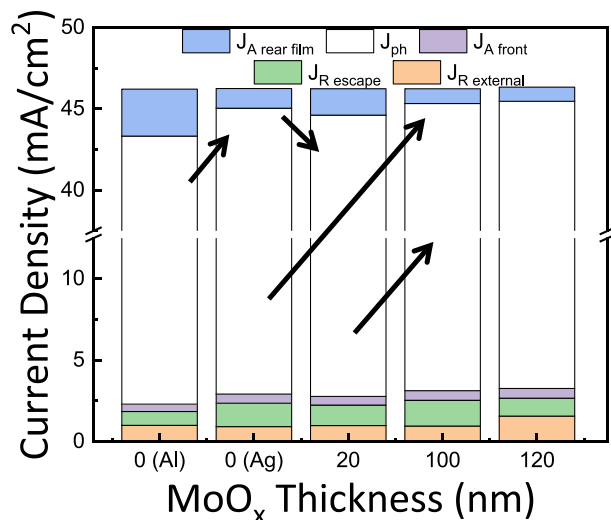


**FIGURE 11** Simulated generated photocurrent density ( $J_{ph}$ ) and current losses due to absorption by rear film ( $J_{A rear}$ ), absorption by front films ( $J_{A front}$ ), and front side reflection ( $J_{R escape}$  and  $J_{R external}$ ). Arrows are to show the increase or decrease in  $J_{ph}$  by varying rear contact stack

recombination losses which explains the inferior infrared EQE of the cell with rear Ag. In conventional solar cells, the back surface usually comprises heavily doped Si for subsequent majority carrier collection and to reduce resistive losses. Such heavily doped region, formed by Al doping or thin doped Si layers, induces free carrier absorption resulting in inherent parasitic light absorption in the infrared. In addition, Al usually used for ohmic-contact formation is a high absorption metal resulting in high current loss ( $J_{A rear film}$ ) as seen in Figure 11. These drawbacks are omitted by using hole-selective MoO<sub>x</sub> at the rear which simultaneously removes the need for heavy doping without sacrificing efficient carrier transport (low contact resistivity) and allows the use of less absorbing metal such as Ag. Therefore, solar cells with MoO<sub>x</sub> placed at the rear have the potential to enable higher  $J_{sc}$ . A further advancement of solar cells with rear MoO<sub>x</sub>/Ag is to fully screen rear side parasitic plasmonic absorption to improve the EQE response in the infrared. Compared with 20 nm, decreasing MoO<sub>x</sub> thickness to 5 and 10 nm reduces the simulated absorption by rear films which is associated with enhanced absorption in Si and escaped light and furthermore yields lower values than the cell with only Ag. Also, thinner MoO<sub>x</sub> enables lower contact resistivity values and thus slightly better FF (SEGA has shown that the corresponding potential efficiency gain is only 0.1%). In practice, unfortunately, our research group has demonstrated that depositing MoO<sub>x</sub> layers with thicknesses  $\leq 10$  nm using the thermal evaporation system is accompanied with surface covering issues resulting in local Si–Ag contacts with high surface recombination and electrical losses that limit overall device performance.<sup>8,64</sup> At this point, depositing ultra-thin MoO<sub>x</sub> layers by ALD may solve this issue. Setting MoO<sub>x</sub> thickness to 50 nm resulted in simulated optical response similar to that of Ag. Figure 10F shows that increasing MoO<sub>x</sub> thickness to  $>50$  nm results in decreased simulated rear side parasitic absorption compared with only

Ag. Consequently, a striking increase in simulated absorption in Si, increase in overall  $J_{ph}$  (Figure 11), and escape reflection in the infrared is observed. By assuming simulated  $J_{ph}$  of 42.2 mA/cm<sup>2</sup> for 100-nm-thick MoO<sub>x</sub> together with experimental  $V_{oc}$  of 626 mV and conserved FF of 76.63%, a maximum  $\eta$  of 20.24% is estimated. These results clearly demonstrate that a rather thick MoO<sub>x</sub> (e.g.,  $\geq 100$  nm) is necessary to fully block the excitation of surface plasmon polaritons thanks to its low refractive index value and thus improve infrared light back reflection in Si and subsequent absorption. However, MoO<sub>x</sub> has high bulk resistivity, and layers with large thicknesses will result in detrimental resistive and electrical losses hindering efficient majority carrier transport.<sup>44</sup> Therefore, thin MoO<sub>x</sub> layer may be used in stack with different dielectric materials with low refractive index, but without incurring resistive and electrical losses, in similar rear side designs such as that of PERC.

## 4 | CONCLUSION

Hole-selective room temperature thermally evaporated MoO<sub>x</sub>/Ag stack was effectively used at the rear of industrial scale p-type c-Si solar cells. The low contact resistivity of Ag/MoO<sub>x</sub> (22 nm)/p-type c-Si clearly demonstrates the effectiveness of MoO<sub>x</sub> as hole-selective contact. Although MoO<sub>x</sub>/Ag-based solar cell has attained an efficiency of 17.65%, this value has to be further improved to competitive levels. By completing SEGA, the efficiency difference between the fabricated solar cell and the theoretical maximum possible efficiency were explained. Based on these analyses, two dominant loss mechanisms are found to obstruct higher efficiency. The first one is due to the synergetic effect of different optical losses which are mainly front metal grid shadowing and front and rear surface reflection losses. Despite the low refractive index of MoO<sub>x</sub> which is necessary to reduce rear side parasitic plasmonic absorption by the rear metal, we found that only 20-nm-thick MoO<sub>x</sub> is not enough to improve the optical response in the infrared. Theoretically, a rather thick MoO<sub>x</sub> layer ( $\geq 100$  nm) is required to enhance internal reflection and absorption in the Si wafer. However, practically such thicknesses block photogenerated carrier transport. On the other hand, further investigation of a rear side stack composed of thin MoO<sub>x</sub> and a low refractive index material that simultaneously allows efficient carrier transport and totally screen parasitic plasmonic absorption is yet to be demonstrated. More importantly, utilizing only a few nanometer of MoO<sub>x</sub> at the rear eliminates the need of doped Si layers with high parasitic free carrier absorption, and further allows the use of less absorbing Ag compared with highly absorbing Al. Although the contribution of individual recombination losses of front and rear surfaces seems to be weaker, their synergetic effect appears as the second dominating loss mechanism. In future works, the possibility to improve front surface passivation and to insert an effective surface passivation interlayer between p-type wafer and MoO<sub>x</sub> to further increase  $V_{oc}$  should be considered. The results shown here suggest that solar cells with remarkable efficiency values can be realized from the proposed design at industrial scale. Finally, this study reveals that SEGA can be utilized as one of the

reliable methods to specify the influence of different layers' properties on the overall performance of solar cells featuring the recently developed hole-selective  $\text{MoO}_x$ . This can be extended to different electrons and hole-selective contacts by adequately defining their corresponding optical, electrical, and passivation properties.

## ACKNOWLEDGEMENTS

This work was supported by the Scientific and Technological Research Council of Turkey (TÜBİTAK) (grant numbers 217M203 and 217M087).

## ORCID

Hisham Nasser  <https://orcid.org/0000-0001-5122-001X>

Mona Zolfaghari Borra  <https://orcid.org/0000-0003-2276-3490>

Emel Semiz  <https://orcid.org/0000-0002-1219-2201>

Raşit Turan  <https://orcid.org/0000-0002-2612-8972>

## REFERENCES

- Shockley W, Queisser HJ. Detailed balance limit of efficiency of  $p$ - $n$  junction solar cells. *J Appl Phys*. 1961;32(3):510-519. <https://doi.org/10.1063/1.1736034>
- Yoshikawa K, Yoshida W, Irie T, et al. Exceeding conversion efficiency of 26% by heterojunction interdigitated back contact solar cell with thin film Si technology. *Sol Energy Mater Sol Cells*. 2017;173(April): 37-42. <https://doi.org/10.1016/j.solmat.2017.06.024>
- Haase F, Hollemann C, Schäfer S, et al. Laser contact openings for local poly-Si-metal contacts enabling 26.1%-efficient POLO-IBC solar cells. *Sol Energy Mater Sol Cells*. 2018;186(March):184-193. <https://doi.org/10.1016/j.solmat.2018.06.020>
- Yang X, Weber K, Hameiri Z, De Wolf S. Industrially feasible, dopant-free, carrier-selective contacts for high-efficiency silicon solar cells. *Prog Photovoltaics Res Appl*. 2017;25(11):896-904. <https://doi.org/10.1002/pip.2901>
- Ahiboz D, Nasser H, Aygün E, Bek A, Turan R. Electrical response of electron selective atomic layer deposited  $\text{TiO}_{2-x}$  heterocontacts on crystalline silicon substrates. *Semicond Sci Technol*. 2018;33(4):1-8, 045013. <https://doi.org/10.1088/1361-6641/aab535>
- Bullock J, Wan Y, Xu Z, et al. Stable dopant-free asymmetric heterocontact silicon solar cells with efficiencies above 20%. *ACS Energy Lett*. 2018;3(3):508-513. <https://doi.org/10.1021/acsenenergylett.7b01279>
- Wang W, He J, Yan D, et al. 21.3%-efficient n-type silicon solar cell with a full area rear  $\text{TiO}_x/\text{LiF}/\text{Al}$  electron-selective contact. *Sol Energy Mater Sol Cells*. 2019;206:1-4, 110291. <https://doi.org/10.1016/j.solmat.2019.110291>
- Nasser H, Kökbudak G, Mehmood H, Turan R. Dependence of n-cSi/ $\text{MoO}_x$  heterojunction performance on cSi doping concentration. *Energy Procedia*. 2017;124:418-424. <https://doi.org/10.1016/j.egypro.2017.09.267>
- Almora O, Gerling LG, Voz C, Alcubilla R, Puigdollers J, Garcia-Belmonte G. Superior performance of  $\text{V}_2\text{O}_5$  as hole selective contact over other transition metal oxides in silicon heterojunction solar cells. *Sol Energy Mater Sol Cells*. 2017;168:221-226. <https://doi.org/10.1016/j.solmat.2017.04.042>
- Yang X, Liu W, De Bastiani M, et al. Dual-function electron-conductive, hole-blocking titanium nitride contacts for efficient silicon solar cells. *Joule*. 3(5):1314-1327. <https://doi.org/10.1016/j.joule.2019.03.008>
- Bullock J, Hettick M, Geissbühler J, et al. Efficient silicon solar cells with dopant-free asymmetric heterocontacts. *Nat Energy*. 2016;1(3): 15031-1-15031-7. <https://doi.org/10.1038/nenergy.2015.31>
- Mehmood H, Nasser H, Tauqeer T, Turan R. Simulation of silicon heterostructure solar cell featuring dopant-free carrier-selective molybdenum oxide and titanium oxide contacts. *Renew Energy*. 2019; 143:359-367. <https://doi.org/10.1016/j.renene.2019.05.007>
- Baker-Finch SC, McIntosh KR, Yan D, Fong KC, Kho TC. Near-infrared free carrier absorption in heavily doped silicon. *J Appl Phys*. 2014;116(6):063106-1-063106-12. <https://doi.org/10.1063/1.4893176>
- Allen TG, Bullock J, Yang X, Javey A, De Wolf S. Passivating contacts for crystalline silicon solar cells. *Nat Energy*. 2019;4(11):914-928. <https://doi.org/10.1038/s41560-019-0463-6>
- Richter A, Glunz SW, Werner F, Schmidt J, Cuevas A. Improved quantitative description of Auger recombination in crystalline silicon. *Phys Rev B—Condens Matter Mater Phys*. 2012;86(16):1-14. <https://doi.org/10.1103/PhysRevB.86.165202>
- Bullock J, Wan Y, Hettick M, et al. Survey of dopant-free carrier-selective contacts for silicon solar cells. In: 2017 IEEE 44th Photovoltaic Specialist Conference, PVSC 2017. Institute of Electrical and Electronics Engineers Inc.; 2017:1-5. <https://doi.org/10.1109/PVSC.2017.8366502>
- Tiwari P, Patel K, Krishnia L, Kumari R, Tyagi PK. Potential application of multilayer n-type tungsten diselenide ( $\text{WSe}_2$ ) sheet as transparent conducting electrode in silicon heterojunction solar cell. *Comput Mater Sci*. 2017;136:102-108. <https://doi.org/10.1016/j.commatsci.2017.04.026>
- Smit S, Garcia-Alonso D, Bordihn S, Hanssen MS, Kessels WMM. Metal-oxide-based hole-selective tunneling contacts for crystalline silicon solar cells. *Sol Energy Mater Sol Cells*. 2014;120(PART A): 376-382. <https://doi.org/10.1016/j.solmat.2013.06.016>
- Essig S, Dréon J, Werner J, et al.  $\text{MoO}_x$  and  $\text{WO}_x$  based hole-selective contacts for wafer-based Si solar cells
- Benick J, Steinhauser B, Muller R, et al. High efficiency n-type PERT and PERL solar cells. 2014 IEEE 40th Photovolt Spec Conf PVSC 2014. 2014:3637-3640. <https://doi.org/10.1109/PVSC.2014.6924895>
- Allen TG, Bullock J, Zheng P, et al. Calcium contacts to n-type crystalline silicon solar cells. *Prog Photovoltaics Res Appl*. 2017;25(7): 636-644. <https://doi.org/10.1002/pip.2838>
- Cho J, Nawal N, Hadipour A, et al. Interface analysis and intrinsic thermal stability of  $\text{MoO}_x$  based hole-selective contacts for silicon heterojunction solar cells. *Sol Energy Mater Sol Cells*. 2019;201:1-9, 110074. <https://doi.org/10.1016/j.solmat.2019.110074>
- Melskens J, Van De Loo BWH, Macco B, Black LE, Smit S, Kessels WMM. Passivating contacts for crystalline silicon solar cells: from concepts and materials to prospects. *IEEE J Photovoltaics*. 2018; 8(2):373-388. <https://doi.org/10.1109/JPHOTOV.2018.2797106>
- Dréon J, Jeangros Q, Cattin J, Haschke J, Antognini L. 23.5%-efficient silicon heterojunction silicon solar cell using molybdenum oxide as hole-selective contact. *Nano Energy*. 2020;1-7, 104495. <https://doi.org/10.1016/j.nanoen.2020.104495>
- Neusel L, Bivour M, Hermle M. Selectivity issues of  $\text{MoO}_x$  based hole contacts. *Energy Procedia*. 2017;124:425-434. <https://doi.org/10.1016/j.egypro.2017.09.268>
- Ahiboz D, Nasser H, Turan R. Admittance analysis of thermally evaporated-hole selective  $\text{MoO}_3$  on crystalline silicon. *Proc 2016 Int Renew Sustain Energy Conf IRSEC 2016*. 2017:144-151. <https://doi.org/10.1109/IRSEC.2016.7983991>
- Bivour M, Macco B, Temmler J, Kessels WMM, Hermle M. Atomic layer deposited molybdenum oxide for the hole-selective contact of silicon solar cells. *Energy Procedia*. 2016;92:443-449. <https://doi.org/10.1016/j.egypro.2016.07.125>
- Mehmood H, Bektaş G, Yıldız İ, Tauqeer T, Nasser H, Turan R. Electrical, optical and surface characterization of reactive RF magnetron sputtered molybdenum oxide films for solar cell applications. *Mater Sci Semicond Process*. 2019;101(May):46-56. <https://doi.org/10.1016/j.mssp.2019.05.018>

29. Lu C, Rusli R, Prakoso AB, Wang H. Carrier selective solution processed molybdenum oxide silicon heterojunctions solar cells with over 12% efficiency. *Semicond Sci Technol*. 2020;35(7):1-6, 075022. <https://doi.org/10.1088/1361-6641/ab8c29>
30. Mehmood H, Nasser H, Ozkol E, Tauqeer T, Hussain S, Turan R. Physical device simulation of partial dopant-free asymmetric silicon heterostructure solar cell (P-DASH) based on hole-selective molybdenum oxide ( $\text{MoO}_x$ ) with Crystalline Silicon (cSi). *Proc 2017 Int Conf Eng Technol ICET 2017*. 2018;2018 January:1-6. <https://doi.org/10.1109/ICEngTechnol.2017.8308155>
31. Mehmood H, Nasser H, Tauqeer T, Hussain S, Ozkol E, Turan R. Simulation of an efficient silicon heterostructure solar cell concept featuring molybdenum oxide carrier-selective contact. *Int J Energy Res*. 2018;42(4):1563-1579. <https://doi.org/10.1002/er.3947>
32. Sen MA, Spinelli P, Kikkert B, et al. Electron beam evaporated molybdenum oxide as hole-selective contact in 6-inch c-Si heterojunction solar cells. *AIP Conf Proc*. 2018;1999(August):1-6. <https://doi.org/10.1063/1.5049264>
33. Spinelli P, Sen MA, Hoek EG, et al. Moly-poly solar cell: Industrial application of metal-oxide passivating contacts with a starting efficiency of 18.1%. *AIP Conf Proc* 2018;1999(August). <https://doi.org/10.1063/1.5049284>
34. Bullock J, Samundsett C, Cuevas A, Yan D, Wan Y, Allen T. Proof-of-concept p-type silicon solar cells with molybdenum oxide local rear contacts. *IEEE J Photovoltaics*. 2015;5(6):1591-1594. <https://doi.org/10.1109/JPHOTOV.2015.2478026>
35. Bullock J, Yan D, Cuevas A, Wan Y, Samundsett C. N- and p-typesilicon solar cells with molybdenum oxide hole contacts. In: *Energy Procedia*. Vol 77. Elsevier Ltd; 2015:446-450. <https://doi.org/10.1016/j.egypro.2015.07.063>
36. Fell A. A free and fast three-dimensional/two-dimensional solar cell simulator featuring conductive boundary and quasi-neutrality approximations. *IEEE Trans Electron Devices*. 2013;60(2):733-738. <https://doi.org/10.1109/TED.2012.2231415>
37. Fell A, McIntosh KR, Altermatt PP, et al. Fell Silicon. *IEEE J Photovoltaics*. 2015;5(4):1250-1263.
38. Abdellaoui T, Bennaceur J, Chtourou R. Effect of nanostructured porous n+ GaAs substrates on the energy band gap of nanocrystalline  $\text{TiO}_2$  thin films analyzed by spectroscopic ellipsometry. *Phys E Low-Dimensional Syst Nanostructures*. 2010;43(1):239-247. <https://doi.org/10.1016/j.jphyse.2010.07.014>
39. Dai ZH, Zhang RJ, Shao J, et al. Optical properties of zinc-oxide films determined using spectroscopic ellipsometry with various dispersion models. *J Korean Phys Soc*. 2009;55(3):1227-1232. <https://doi.org/10.3938/jkps.55.1227>
40. Cox RH, Strack H. Ohmic contacts for GaAs devices. *Solid State Electron*. 1967;10(12):1213-1218. [https://doi.org/10.1016/0038-1101\(67\)90063-9](https://doi.org/10.1016/0038-1101(67)90063-9)
41. Wang W, Lin H, Yang Z, et al. An expanded Cox and Strack method for precise extraction of specific contact resistance of transition metal oxide/n-silicon heterojunction. *IEEE J Photovoltaics*. 2019;9(4):1113-1120. <https://doi.org/10.1109/JPHOTOV.2019.2917386>
42. Gerling LG, Voz C, Alcubilla R, Puigdollers J. Origin of passivation in hole-selective transition metal oxides for crystalline silicon heterojunction solar cells. *J Mater Res*. 2017;32(2):260-268. <https://doi.org/10.1557/jmr.2016.453>
43. Kane DE, Swanson RM. Measurement of the emitter saturation current by a contactless photoconductivity decay method. In: *Conference Record of the IEEE Photovoltaic Specialists Conference*. IEEE; 1985:578-583.
44. Bullock J, Cuevas A, Allen T, Battaglia C. Molybdenum oxide  $\text{MoO}_x$ : a versatile hole contact for silicon solar cells. *Appl Phys Lett*. 2014;105(23):232109-1-232109-5. <https://doi.org/10.1063/1.4903467>
45. Mader C, Müller J, Eidelloth S, Brendel R. Local rear contacts to silicon solar cells by in-line high-rate evaporation of aluminum. *Sol Energy Mater Sol Cells*. 2012;107:272-282. <https://doi.org/10.1016/j.solmat.2012.06.047>
46. Greiner MT, Chai L, Helander MG, Tang WM, Lu ZH. Metal/metal-oxide interfaces: how metal contacts affect the work function and band structure of  $\text{MoO}_3$ . *Adv Funct Mater*. 2013;23(2):215-226. <https://doi.org/10.1002/adfm.201200993>
47. Mehmood H, Nasser H, Tauqeer T, Turan R. Numerical analysis of silicon heterojunction solar cell based on molybdenum oxide as a back surface field (BSF). *Proc 33rd Eur Photovolt Sol Energy Conf Exhib 25-29 Sept 2017, Amsterdam, Holl*. 2017;(November):932-936. <https://doi.org/10.4229/EUPVSEC20172017-2CV.2.66>
48. Eectr E. Characterization of alternative carrier selective materials and their application to heterojunction solar cells. 2017.
49. Sun T, Wang R, Liu R, et al. Investigation of  $\text{MoO}_x$ /n-Si strong inversion layer interfaces via dopant-free heterocontact. *Phys Status Solidi Rapid Res Lett*. 2017;11(7):1-6. <https://doi.org/10.1002/pssr.201700107>
50. Gerling LG, Mahato S, Morales-Vilches A, et al. Transition metal oxides as hole-selective contacts in silicon heterojunctions solar cells. *Sol Energy Mater Sol Cells*. 2016;145:109-115. <https://doi.org/10.1016/j.solmat.2015.08.028>
51. Es F, Semiz E, Orhan E, et al. Optimization of PERC fabrication based on loss analysis in an industrially relevant environment: first results from GüNAM photovoltaic line (GPVL). *Renew Energy*. 2020;146:1676-1681. <https://doi.org/10.1016/j.renene.2019.07.149>
52. Brendel R, Dullweber T, Peibst R, Kranz C, Merkle A, Walter D. Breakdown of the efficiency gap to 29% based on experimental input data and modeling. *Prog Photovoltaics Res Appl*. 2016;24(12):1475-1486. <https://doi.org/10.1002/pip.2696>
53. Cho JS, Jang E, Lim D, et al. Performance enhancement of thin-film silicon solar cells by development of core component layers. *Sol Energy*. 2018;159:444-452. <https://doi.org/10.1016/j.solener.2017.11.025>
54. Özkol E, Procel P, Zhao Y, et al. Effective passivation of black silicon surfaces via plasma-enhanced chemical vapor deposition grown conformal hydrogenated amorphous silicon layer. *Phys Status Solidi Rapid Res Lett*. 2020;14(1):1-7. <https://doi.org/10.1002/pssr.201900087>
55. Herasimenka SY, Dauksher WJ, Bowden SG. >750 mV open circuit voltage measured on 50  $\mu\text{m}$  thick silicon heterojunction solar cell. *Appl Phys Lett*. 2013;103(5):053511-1-053511-4. <https://doi.org/10.1063/1.4817723>
56. Schmidt J, Peibst R, Brendel R. Surface passivation of crystalline silicon solar cells: present and future. *Sol Energy Mater Sol Cells*. 2018;187(May):39-54. <https://doi.org/10.1016/j.solmat.2018.06.047>
57. Kim M, Park S, Kim D. Highly efficient PERC cells fabricated using the low cost laser ablation process. *Sol Energy Mater Sol Cells*. 2013;117:126-131. <https://doi.org/10.1016/j.solmat.2013.04.025>
58. Min B, Müller M, Wagner H, et al. A roadmap toward 24% efficient PERC solar cells in industrial mass production. *IEEE J Photovoltaics*. 2017;7(6):1541-1550. <https://doi.org/10.1109/JPHOTOV.2017.2749007>
59. Larionova Y, Turcu M, Reiter S, et al. On the recombination behavior of p+-type polysilicon on oxide junctions deposited by different methods on textured and planar surfaces. *Phys Status Solidi Appl Mater Sci*. 2017;214(8):1-5. <https://doi.org/10.1002/pssa.201700058>
60. Rienacker M, Bossmeyer M, Merkle A, et al. Junction resistivity of carrier selective polysilicon on oxide junctions and its impact on the solar cell performance. 2017 IEEE 44th Photovolt Spec Conf PVSC 2017. 2017;7(1):1-7. 10.1109/PVSC.2017.8366491
61. Wafer Ray Tracer. <https://www2.pvlighthouse.com.au/calculators/waferraytracer/wafer-ray-tracer.html>. Accessed March 27, 2020.
62. Holman ZC, Filipič M, Lipovšek B, et al. Parasitic absorption in the rear reflector of a silicon solar cell: simulation and measurement of the sub-bandgap reflectance for common dielectric/metal reflectors.

- Sol Energy Mater Sol Cells*. 2014;120(Part A):426-430. <https://doi.org/10.1016/j.solmat.2013.06.024>
63. Holman ZC, De Wolf S, Ballif C. Improving metal reflectors by suppressing surface plasmon polaritons: a priori calculation of the internal reflectance of a solar cell. *Light Sci Appl*. 2013;2:e106-1-e106-6. <https://doi.org/10.1038/lsa.2013.62>
64. Akdemir O, Zolfaghari Borra M, Nasser H, Turan R, Bek A. MoO<sub>x</sub>/Ag/MoO<sub>x</sub> multilayers as hole transport transparent conductive electrodes for n-type crystalline silicon solar cells. *Int J Energy Res*. December 2019;2020:1-12. <https://doi.org/10.1002/er.5145>
65. Sproul AB. Dimensionless solution of the equation describing the effect of surface recombination on carrier decay in semiconductors. *J Appl Phys*. 1994;76(5):2851-2854. <https://doi.org/10.1063/1.357521>
66. Horbelt R, Micard G, Keller P, Job R, Hahn G, Terheiden B. Surface recombination velocity of local Al-contacts of PERC solar cells

determined from LBIC measurements and 2D simulation. *Energy Procedia*. 2016;92:82-87. <https://doi.org/10.1016/j.egypro.2016.07.033>

#### SUPPORTING INFORMATION

Additional supporting information may be found online in the Supporting Information section at the end of this article.

**How to cite this article:** Nasser H, Es F, Zolfaghari Borra M, et al. On the application of hole-selective MoO<sub>x</sub> as full-area rear contact for industrial scale p-type c-Si solar cells. *Prog Photovolt Res Appl*. 2020;1-13. <https://doi.org/10.1002/pip.3363>